Linear ion trap imperfection and the compensation of excess micromotion*

Xie Yi(谢 艺)[a)b)], Wan Wei(万 威)[a)b)], Zhou Fei(周 飞)[a)],
Chen Liang(陈 亮)[a)], Li Chao-Hong(李朝红)[c)], and Feng Mang(冯 芒)[a)†]

[a)] *State Key Laboratory of Magnetic Resonance and Atomic and Molecular Physics, Wuhan Institute of Physics and Mathematics, Chinese Academy of Sciences, and Wuhan National Laboratory for Optoelectronics, Wuhan* 430071, *China*
[b)] *Graduate School of the Chinese Academy of Sciences, Beijing* 100049, *China*
[c)] *State Key Laboratory of Optoelectronic Materials and Technologies, School of Physics and Engineering, Sun Yat-Sen University, Guangzhou* 510275, *China*

(Received 30 November 2011; revised manuscript received 5 January 2012)

Quantum computing requires ultracold ions in a ground vibrational state, which is achieved by sideband cooling. We report our recent efforts towards the Lamb–Dicke regime which is a prerequisite of sideband cooling. We first analyse the possible imperfection in our linear ion trap setup and then demonstrate how to suppress the imperfection by compensating the excess micromotion of the ions. The ions, after the micromotion compensation, are estimated to be very close to the Doppler-cooling limit.

Keywords: trapped ions, micromotion, compensation

PACS: 32.80.Wr, 03.67.Lx, 32.70.Jz, 42.62.Fi **DOI:** 10.1088/1674-1056/21/6/063201

1. Introduction

Among the candidates for quantum information processing (QIP), trapped ions are most promising due to full controllability of the ionic qubits and the long coherence time of the ionic states.[1−5] The original idea came Cirac and Zoller's proposal,[6] in which the qubits are encoded into the internal states of the ions and the common quantized vibrational modes are used for coupling the qubits. To realize the idea, we have to first achieve the cooling of the vibrational states of the ions to the ground state. The cooling consists of two steps, i.e., Doppler cooling and sideband cooling.[7,8] The former could cool the ions to be within the Lamb–Dicke regime and the latter achieves the ground vibrational state of the ions.[9]

However, the ion trap suffers from imperfections due to misalignment of the endcap electrodes, the uneven coating of calcium (also called patch effects), the deposit of electrons on the electrodes and the radio frequency (RF) inductive voltage in the DC electrodes. These negative effects heat the trapped ions and hinder the cooling towards the Lamb–Dicke regime. We report in this paper our recent effort in our home-built linear ion trap to minimize the negative effects due to imperfection of the trap and to cool the trapped $^{40}Ca^{+}$ ions reaching the Lamb–Dicke regime.

As presented previously, we have achieved in our linear ion-trap setup the photoionization and the stable confinement of a string of ions by micromotion compensation,[10] and have also measured some typical characteristic parameters.[11] In that work, however, the compensation was accomplished only in one of the radial directions and the RF inductive voltage was not well suppressed. So the ions were still confined much beyond the Doppler-cooling limit, which hinders us in carrying out sideband cooling. We demonstrate below our recent work on the compensation for the excess micromotion in all dimensions and the suppression of the RF inductive voltage. A much narrower linewidth of the excitation spectrum of the trapped $^{40}Ca^{+}$ ions has been obtained. We also estimate the negative effects left in our setup and the misalignment of the trap structure. Our calculation indicates that the Lamb–Dicke regime has been reached in our linear ion trap.

This paper is structured as follows. We first the-

*Project supported by the National Natural Science Foundation of China (Grants Nos. 10974225 and 11104325), the NCETPC (Grant No. NCET-10-0850), the Fundamental Research Funds for Central Universities of China, and the National Fundamental Research Program of China (Grant No. 2012CB922102).

†Corresponding author. E-mail: mangfeng@wipm.ac.cn

© 2012 Chinese Physical Society and IOP Publishing Ltd

oretically analyse the origin of the excess micromotion and the method of micromotion compensation. Then we report our experimental effort for compensating the excess micromotion and for measuring different characteristic parameters. Some discussions and a brief conclusion are given in the final section.

2. Theory of the linear ion trap

2.1. Basic equations for the trapped ions

The linear ion trap in our experiment has been described in Ref. [12] and shown in Fig. 1(a), where the blade-like electrodes provide RF: electrodes 1 and 3 are connected to the ground and electrodes 2 and 4 produce the potential $V\cos(\Omega t)$ with $\Omega/2\pi =$ 20.1 MHz. So the potential due to the electrodes near the trap axis is

$$\Phi_{\rm rf}(x,y,t) = \frac{\alpha_{\rm ac}V}{2}\left(1+\frac{x^2-y^2}{{r_0}^2}\right)\cos(\Omega t), \qquad (1)$$

where r_0 is the perpendicular distance from the trap axis to the RF electrodes and $\alpha_{\rm ac}(<1)$ is an RF geometrical factor. In addition, a harmonic pseudopotential

$$\Phi_{\rm ec}(x,y,z) = \frac{\kappa U_{\rm ec}}{L^2}\left[z^2-\frac{1}{2}(x^2+y^2)\right] \qquad (2)$$

is created by the static voltage $U_{\rm ec}$ near the center of the trap, where $\kappa(<1)$ is an axial geometrical factor and L is half of the length between the two endcaps. As a result, the total potential is given by $\Phi = \Phi_{\rm rf} + \Phi_{\rm ec}$.

Accordingly the total electric field is

$$\begin{aligned}\boldsymbol{E}(x,y,z,t) &= -V\left(\frac{x\hat{x}-y\hat{y}}{r_0^2}\right)\cos(\Omega t)\\ &\quad -\frac{\kappa U_{\rm ec}}{L^2}(2z\hat{z}-x\hat{x}-y\hat{y}), \qquad (3)\end{aligned}$$

and the motion of a single ion of mass m and charge Q in above field is determined by the Mathieu equation

$$\ddot{u}_i + [a_i + 2q_i\cos(\Omega t)]\frac{\Omega^2}{4}u_i = 0, \qquad (4)$$

where $u = u_x\hat{x} + u_y\hat{y} + u_z\hat{z}$ is the position of the ion using the coordinate system shown in Fig. 1(b), and the parameters are defined by

$$\begin{aligned}a_x = a_y = -\frac{1}{2}a_z = -\frac{4Q\kappa U_{\rm ec}}{mL^2\Omega^2},\\ q_x = -q_y = -\frac{2Q\alpha_{\rm ac}V}{mr_0^2\Omega^2}, \quad q_z = 0. \qquad (5)\end{aligned}$$

For convenience, we define the unit vectors $\hat{u}_x = \hat{x}$, $\hat{u}_y = \hat{y}$, and $\hat{u}_z = \hat{z}$.

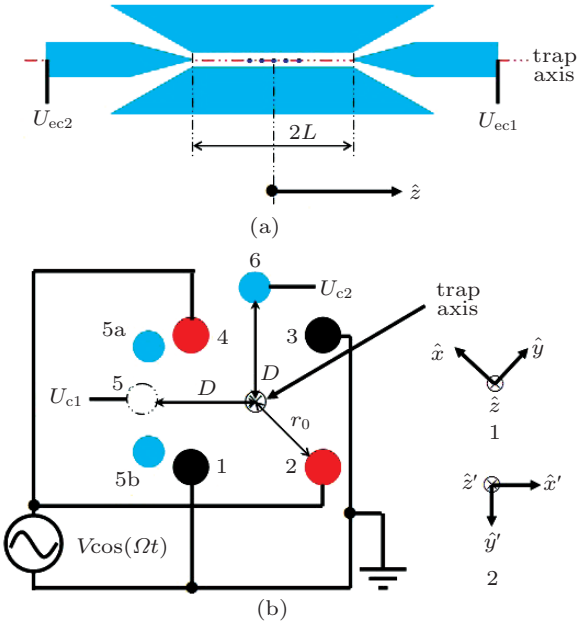


Fig. 1. (colour online) The schematic of a linear ion trap, where $r_0 = 0.9$ mm, $D = 7$ mm, $L = 2.5$ mm. For clarity, r_0 is magnified in the plot with respect to the real size. Panel (a) is the side view. The trap axis is along the z direction, and the origin is centered between the two endcaps; panel (b) is the axial view. The blade-like RF electrodes (labeled as 1–4) are represented by four filled circles in red and black. The compensation electrodes 5 (separated as 5a and 5b) and 6 are plotted as blue filled circles. The endcaps are omitted for clarity. For convenience of description, we take two coordinate systems, where x and y axes are along the diagonal RF electrodes, respectively, and x' and y' axes are along the horizontal and vertical directions, respectively. The z (z') axis represents the trap axis.

Since $|q_i| \ll 1$ and $|a_i| \ll 1$ are always satisfied experimentally, we could only consider the first-order solution to Eq. (4) as $u_i(t) \approx u_{1i}\cos(\omega_i t + \varphi_{Si})[1 + (q_i/2)\cos(\Omega t)]$ (Ref. [13]) with the phase φ_{Si} and

$$\omega_i \cong \frac{\Omega}{2}\sqrt{a_i + \frac{1}{2}q_i^2}. \qquad (6)$$

For N ions trapped under the condition of $(\omega_z/\omega_r)^2 \le 2.53N^{-1.73}$,[14] the ions are strongly bounded in the radial directions, and only weakly bounded in the axial direction, which result in a linear chain geometry. The equilibrium positions (z_i for the i-th ion) are given by the minima of the potential energy[15]

$$E_p = \sum_{j=1}^{N}\frac{m}{2}\omega_z^2 z_j^2 + \sum_{i,j=1,i\neq j}^{N}\frac{Q^2}{8\pi\epsilon_0}\frac{1}{|z_j - z_i|}. \qquad (7)$$

2.2. The effect of extra uniform static electric field and the compensation

If the trapped ion is subject to an extra uniform static electric field $\boldsymbol{E}_{\rm dc}$, Eq. (4) becomes

$$\ddot{u}_i + [a_i + 2q_i\cos(\Omega t)]\frac{\Omega^2}{4}u_i = \frac{Q\boldsymbol{E}_{\rm dc}\cdot\hat{u}_i}{m}. \quad (8)$$

To the lowest order in a_i and q_i, the solution to Eq. (8) is[13]

$$u_i(t) \approx [u_{0i} + u_{1i}\cos(\omega_i t + \varphi_{Si})]\left[1 + \frac{q_i}{2}\cos(\Omega t)\right], \quad (9)$$

with

$$u_{0i} \cong \frac{Q\boldsymbol{E}_{\rm dc}\cdot\hat{u}_i}{m\omega_i^2}.$$

The field $\boldsymbol{E}_{\rm dc}$ displaces the average position of the ion and causes excess micromotion with the amplitude $\frac{1}{2}u_{0i}q_i$ along $\hat{u}_i$, which handicaps the efficiency of the laser cooling.

The stray electric field is associated with the misalignment of the endcap electrodes, the uneven coating of calcium and the deposit of electrons on the electrodes. The former two factors can be easily distinguished from each other because the stray electric field caused by misalignment varies with the endcap voltage, but the other keeps constant. The deposit of electrons could be neglected in our setup as we employ photoionization, which largely suppresses the deposit of the electrons.

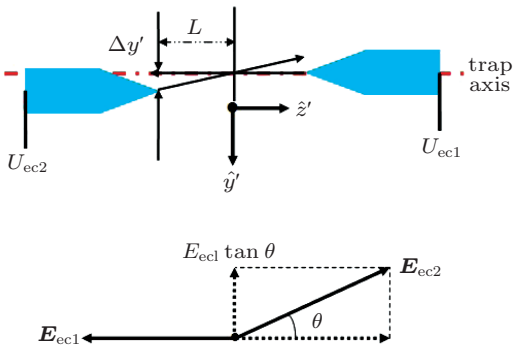


Fig. 2. (colour online) Misalignment of the endcaps, which yields extra components in $\hat{y}'$ and $\hat{x}'$ directions in the case of the electric field applied along $\hat{z}$ direction.

We denote the constant component by $\boldsymbol{E}_{\rm dc1}$, and the endcap-voltage dependent component by $\boldsymbol{E}_{\rm dc2}$, yielding $\boldsymbol{E}_{\rm dc} = \boldsymbol{E}_{\rm dc1} + \boldsymbol{E}_{\rm dc2}$. The small misalignment of endcap 2 $\Delta y'_{\rm ec2}$ (See Fig. 2) causes an extra electric field along the $\hat{y}'$ direction

$$E_{{\rm dc}2y'} = \boldsymbol{E}_{\rm ec2}\cdot\hat{y}' = E_{\rm ec1}\tan\theta \cong E_{\rm ec1}\frac{\Delta y'_{\rm ec2}}{L}$$

and a small misalignment $\Delta x'_{\rm ec2}$ causes an extra electric field along the $\hat{x}'$ direction

$$E_{{\rm dc}2x'} = \boldsymbol{E}_{\rm ec2}\cdot\hat{x}' = E_{\rm ec1}\tan\theta \cong E_{\rm ec1}\frac{\Delta x'_{\rm ec2}}{L}.$$

The excess micromotion in different directions should be compensated in different ways. In the radial direction, excess micromotion can be eliminated by compensating electrodes 5 and 6, which cancel the horizontal and vertical stray fields, respectively. The $\hat{x}'$ and $\hat{y}'$ components of the compensating electric field are $E_{{\rm c}1x'} = \alpha_{\rm c1}U_{\rm c1}/D$ and $E_{{\rm c}2y'} = \alpha_{\rm c2}U_{\rm c2}/D$, respectively,[16] where $U_{\rm c1}$ and $U_{\rm c2}$ are voltages applied to the electrodes 5 and 6, D is the effective distance between the compensating electrode and trap center and $\alpha_{\rm c1}$, $\alpha_{\rm c2}$ are called DC geometrical factors. On the other hand, the axial stray field can be compensated by unequal endcap voltage $E_{{\rm ec}z'} = \alpha_{\rm ec}(U_{\rm ec2} - U_{\rm ec1})/L$. So the well compensated condition in three dimensions is $\boldsymbol{E}_{\rm dc1} + \boldsymbol{E}_{\rm dc2} + E_{{\rm c}1x'}\hat{x}' + E_{{\rm c}2y'}\hat{y}' + E_{{\rm ec}z'}\hat{z}' = 0$.

We have to mention that, although the displacement of the ions in the axial direction does not cause excess micromotion by using $q_z = 0$ in Eq. (9), the ion compensated for the axial stray field does show a better excitation spectrum for the reason discussed in the following sections.

2.3. The effects of the RF phase shift and the RF inductive voltage

Excess micromotion can also be caused by the phase difference $\varphi'_{\rm ac}$ between the ac potentials of the RF electrodes 2 and 4. If $\varphi_{\rm ac} < 1$ rad, the potential of electrode 4 is

$$V\cos\left(\Omega t + \frac{1}{2}\varphi_{\rm ac}\right) \cong V\cos(\Omega t) - \frac{1}{2}V\varphi_{\rm ac}\sin(\Omega t)$$

and the potential of electrode 2 is

$$V\cos\left(\Omega t - \frac{1}{2}\varphi_{\rm ac}\right) \cong V\cos(\Omega t) + \frac{1}{2}V\varphi_{\rm ac}\sin(\Omega t).$$

So the total electric field near the trap center is written as

$$\begin{aligned}\boldsymbol{E}(x,y,z,t) \cong\ & -\frac{V}{r_0^2}(x\hat{x} - y\hat{y})\cos(\Omega t)\\ & -\frac{\kappa U_{\rm ec}}{L^2}(2z\hat{z} - x\hat{x} - y\hat{y})\\ & +\boldsymbol{E}_{\rm dc} + \frac{V\varphi_{\rm ac}\alpha'_{\rm ac}}{2r_0}\sin(\Omega t)\hat{x}, \quad (10)\end{aligned}$$

where $\alpha'_{\rm ac}$ is generally different from $\alpha_{\rm ac}$ but depends on the trap geometry. The equations of motion in $\hat{y}$ and $\hat{z}$ directions remain the same as Eq. (8), but the solution in $\hat{x}$ direction becomes,[13]

$$u_x(t) \approx\ [u_{0x} + u_{1x}\cos(\omega_x t + \varphi_{Sx})]\left[1 + \frac{q_x}{2}\cos(\Omega t)\right]$$

$$-\frac{1}{4}q_x r_0 \alpha'_{\rm ac}\varphi_{\rm ac}\sin(\Omega t). \quad (11)$$

Equation (11) shows that unless $\varphi_{\rm ac}=0$, the excess micromotion in $\hat{x}$ direction would not vanish for any average ion position $\boldsymbol{u}_0$. The phase shift is always expected to be caused by asymmetry in the electric impedances of the electrodes. However, there exists another situation where the RF inductive voltage plays a similar role.

Due to the static electrodes near the blade-like RF electrodes, the RF inductive voltage through capacity coupling is unavoidable, which produces an effective phase shift. We denote the inductive ac voltage on the compensation electrodes 5 and 6 by V_1 and V_2, and denote the corresponding phase shifts by φ_1 and φ_2. The additional electric field due to the induced ac voltage can be expressed as

$$\begin{aligned}\boldsymbol{E}_{\rm ac1} =& \frac{\alpha_{\rm c1}V_1\cos(\Omega t+\varphi_1)}{\sqrt{2}D}(\hat{y}-\hat{x})\\ &-\frac{\alpha_{\rm c1}V_1\cos(\Omega t+\varphi_1)}{\sqrt{2}D^2}(y\hat{y}-x\hat{x}), \quad (12)\\ \boldsymbol{E}_{\rm ac2} =& \frac{\alpha_{\rm c2}V_1\cos(\Omega t+\varphi_2)}{\sqrt{2}D^2}(x\hat{x}+y\hat{y})\\ &-\frac{\alpha_{\rm c2}V_2\cos(\Omega t+\varphi_2)}{\sqrt{2}D}(\hat{x}+\hat{y}). \quad (13)\end{aligned}$$

For $\boldsymbol{E}_{\rm ac1}$ and $\boldsymbol{E}_{\rm ac2}$ in the case $\varphi_1=\varphi_2=0$, equation (10) is rewritten as

$$\begin{aligned}&\boldsymbol{E}(x,y,z,t)\\ =&-\frac{\kappa U_{\rm ec}}{L^2}(2z\hat{z}-x\hat{x}-y\hat{y})+\boldsymbol{E}_{\rm dc}\\ &+\frac{V\varphi_{\rm ac}\alpha'_{\rm ac}}{2r_0}\sin(\Omega t)\hat{x}\\ &+\frac{\alpha_{\rm c1}V_1+\alpha_{\rm c2}V_2}{\sqrt{2}D}\sin(\Omega t)\hat{x}\\ &-\frac{\alpha_{\rm c1}V_1-\alpha_{\rm c2}V_2}{\sqrt{2}D}\sin(\Omega t)\hat{y}\\ &-\left(\frac{\alpha_{\rm ac}V}{r_0^2}-\frac{\alpha_{\rm c1}V_1+\alpha_{\rm c2}V_2}{\sqrt{2}D^2}\right)\cos(\Omega t)x\hat{x}\\ &+\left(\frac{\alpha_{\rm ac}V}{r_0^2}-\frac{\alpha_{\rm c1}V_1-\alpha_{\rm c2}V_2}{\sqrt{2}D^2}\right)\cos(\Omega t)y\hat{y}. \quad (14)\end{aligned}$$

A more complete consideration is taken into account below for the RF inductive voltage by the endcap electrodes. If the inductive voltage of the endcap is $V_{\rm ec}\cos(\Omega t)$, the electric field is

$$\boldsymbol{E}_{\rm ac'}=-\frac{\kappa V_{\rm ec}}{L^2}(2z\hat{z}-x\hat{x}-y\hat{y})\cos(\Omega t).$$

So equation (14) is replaced by

$$\begin{aligned}&\boldsymbol{E}(x,y,z,t)\\ =&-\frac{\kappa U_{\rm ec}}{L^2}(2z\hat{z}-x\hat{x}-y\hat{y})+\boldsymbol{E}_{\rm dc}\\ &+\frac{V\varphi_{\rm ac}\alpha'_{\rm ac}}{2r_0}\sin(\Omega t)\hat{x}\\ &+\frac{\alpha_{\rm c1}V_1+\alpha_{\rm c2}V_2}{\sqrt{2}D}\sin(\Omega t)\hat{x}\\ &-\frac{\alpha_{\rm c1}V_1-\alpha_{\rm c2}V_2}{\sqrt{2}D}\sin(\Omega t)\hat{y}\\ &+\left(\frac{\kappa V_{\rm ec}}{L^2}-\frac{\alpha_{\rm ac}V}{r_0^2}+\frac{\alpha_{\rm c1}V_1+\alpha_{\rm c2}V_2}{\sqrt{2}D^2}\right)\cos(\Omega t)x\hat{x}\\ &+\left(\frac{\kappa V_{\rm ec}}{L^2}+\frac{\alpha_{\rm ac}V}{r_0^2}-\frac{\alpha_{\rm c1}V_1-\alpha_{\rm c2}V_2}{\sqrt{2}D^2}\right)\cos(\Omega t)y\hat{y}\\ &-\frac{2\kappa V_{\rm ec}}{L^2}\cos(\Omega t)z\hat{z}. \quad (15)\end{aligned}$$

We may solve the equations of motion to the lowest order of a_i, q_i, $\varphi_{\rm ac}$, V_1, and V_2, yielding

$$\begin{aligned}u_x(t)\approx&\ [u_{0x}+u_{1x}\cos(\omega_x t+\varphi_{Sx})]\left[1+\frac{q'_x}{2}\cos(\Omega t)\right]\\ &-\frac{1}{4}q_x r_0\alpha'_{\rm ac}\varphi_{\rm ac}\sin(\Omega t)\\ &-\frac{Q}{\sqrt{2}Dm\Omega^2}(\alpha_{c1}V_1+\alpha_{c2}V_2)\sin(\Omega t), \quad (16)\\ u_y(t)\approx&\ [u_{0y}+u_{1y}\cos(\omega_y t+\varphi_{Sy})]\left[1+\frac{q'_y}{2}\cos(\Omega t)\right]\\ &+\frac{Q}{\sqrt{2}Dm\Omega^2}(\alpha_{c1}V_1-\alpha_{c2}V_2)\sin(\Omega t), \quad (17)\\ u_z(t)\approx&\ [u_{0z}+u_{1z}\cos(\omega_z t+\varphi_{Sz})]\\ &\times\left[1+\frac{q'_z}{2}\cos(\Omega t)\right], \quad (18)\end{aligned}$$

where, due to $D,\ L\gg r_0$, under the condition $\alpha_{\rm c1}V_1$, $\alpha_{\rm c2}V_2$, $\kappa V_{\rm ec}\ll\alpha_{\rm ac}V$, we have

$$\begin{aligned}q'_x&=\frac{2Q}{m\Omega^2}\left(\frac{\alpha_{\rm ac}V}{r_0^2}-\frac{\alpha_{\rm c1}V_1+\alpha_{\rm c2}V_2}{\sqrt{2}D^2}-\frac{\kappa V_{\rm ec}}{L^2}\right)\cong q_x,\\ q'_y&=-\frac{2Q}{m\Omega^2}\left(\frac{\alpha_{\rm ac}V}{r_0^2}-\frac{\alpha_{\rm c1}V_1-\alpha_{\rm c2}V_2}{\sqrt{2}D^2}+\frac{\kappa V_{\rm ec}}{L^2}\right)\cong q_y,\\ q'_z&=\frac{4Q}{m\Omega^2}\frac{\kappa V_{\rm ec}}{L^2}\ll q_r,\end{aligned}$$

and a_i, ω_i are defined as given above.

Similar to the excess micromotion caused by ac phase shift, equations (16)–(18) show that the excess micromotion in both $\hat{x}$ and $\hat{y}$ directions would not vanish for any average ion position $\boldsymbol{u}_0$ unless the RF inductive voltage $V_1=V_2=0$. Besides, since $q'_z\neq 0$, the ion displacements in the axial direction will result in an excess micromotion.

From Eqs. (16)–(18), the average kinetic energy due to the motion along the $\hat{u}_i$ direction is

$$\begin{aligned}E_{Ki}\cong&\frac{1}{4}mu_{1i}^2\left(\omega_i^2+\frac{1}{8}q_i^2\Omega^2\right)+\frac{4}{m}\left(\frac{Qq_i\boldsymbol{E}_{\rm dc}\cdot\hat{u}_i}{(2a_i+q_i^2)\Omega}\right)^2\\ &+\left(\frac{1}{64}m(q_x r_0\alpha'_{\rm ac}\varphi_{\rm ac}\Omega)^2\right.\end{aligned}$$

$$+\frac{1}{4m}\left(\frac{Q(\alpha_{c1}V_1+\alpha_{c2}V_2)}{D\Omega}\right)^2\Big)\delta_{i,x}$$
$$+\frac{1}{4m}\left(\frac{Q(\alpha_{c1}V_1-\alpha_{c2}V_2)}{D\Omega}\right)^2\delta_{i,y}. \quad (19)$$

The first term is the kinetic energy of secular motion and micromotion, which can be reduced by laser cooling. The second term is attributed to the excess micromotion caused by a stray static field, which can be suppressed by applying a proper compensation voltage. However, the last two terms can only be suppressed by improving the electric connections and the filter network.

2.4. Detection of micromotion by using the two-dimensional cross-correlation method

Several techniques have been developed to detect excess micromotion.[13] In our previous work,[10] position compensation, linewidth compensation, and cross-correlation method in the $\hat{x}'$ direction have been carried out by using a 397-nm laser and an 866-nm repumping laser (i.e., beam 1 in Fig. 3), and a 22-MHz linewidth excitation spectrum at 397 nm has been achieved. Recently, we employed another Doppler-cooling laser (397-nm laser, i.e., beam 2 in Fig. 3) together with the 866-nm repumping laser to detect and compensate the excess micromotion in the vertical direction and to suppress the inductive voltage, which has achieved an excitation spectrum of (22.9/2)-MHz linewidth.

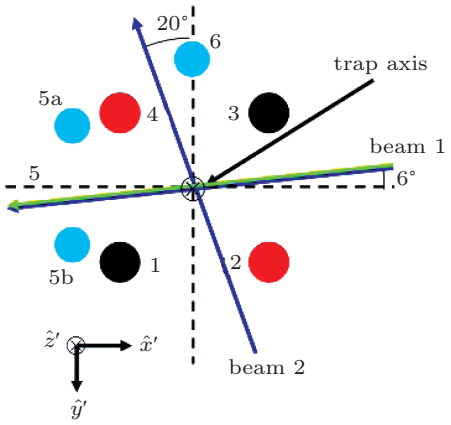


Fig. 3. (colour online) Laser beams for the compensation of micromotion in both $\hat{x}'$ and $\hat{y}'$ directions, where one 397-nm laser and the repumping 866-nm laser are denoted by beam 1, and another 397-nm laser is denoted by beam 2. Both beam 1 and beam 2 hold an angle of about 30° with respect to the trap axis, so the micromotion in $\hat{z}$ direction can also be detected.

Taking all the effects that cause excess micromotion into account, we define

$$\beta=\sqrt{\left(\frac{1}{2}\sum_{i=x,y,z}k_iu_{0i}q_i\right)^2+\left(\frac{1}{4}k_xq_xr_0\alpha'_{ac}\varphi_{ac}+\frac{k_xQ(\alpha_{c1}V_1+\alpha_{c2}V_2)}{\sqrt{2}mD\Omega^2}-\frac{k_yQ(\alpha_{c1}V_1-\alpha_{c2}V_2)}{\sqrt{2}mD\Omega^2}\right)^2} \quad (20)$$

with $\boldsymbol{k}$ being the wave vector. In the frame with an ion undergoing excess micromotion, the laser frequency is Doppler shifted by $-\boldsymbol{k}\cdot\boldsymbol{V}_\mu=\beta\Omega\sin(\Omega t+\delta)$. In the low intensity limit, the detected fluorescence rate is[13]

$$R_d=R_{\max}\frac{(\gamma)^2/2}{(\gamma/2)^2+[\Omega_{atom}-\Omega_{laser}-\beta\Omega\sin(\Omega t+\delta)]^2}. \quad (21)$$

Since beam 1 has barely any action in the vertical direction, excess micromotion in that direction cannot be detected and compensated effectively. As a result, it is the added beam 2 that achieves a more complete compensation.

3. Experimental implementation of compensating excess micromotion and measuring geometrical factors

3.1. Measuring the ion displacements by EMCCD

The displacements of the ions in the trap can be monitored by the EMCCD which is installed by an angle θ_v with respect to the trap axis. The real size of the ions in the trap could be represented by the pixels on the EMCCD camera based on the following method.

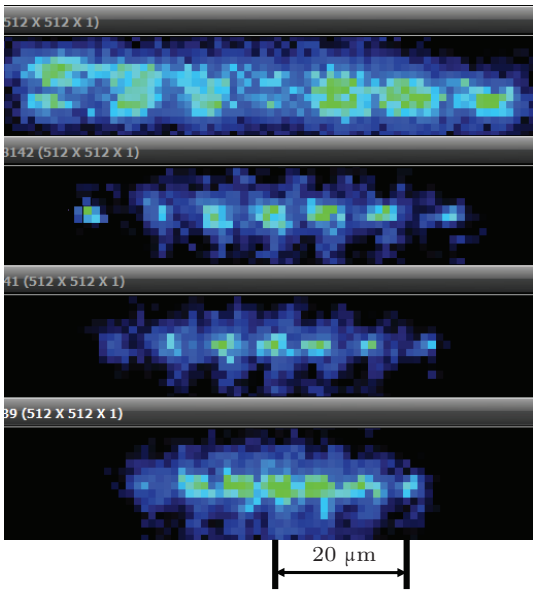


Fig. 4. (colour online) Images obtained under different axial secular frequencies. From the top to bottom ω_z is 150 kHz, 207 kHz, 259 kHz, and 334 kHz, respectively. Larger secular frequency is not used for better accuracy. The image in the top is blurry because the ions are out of the optimal object area of the imaging system.

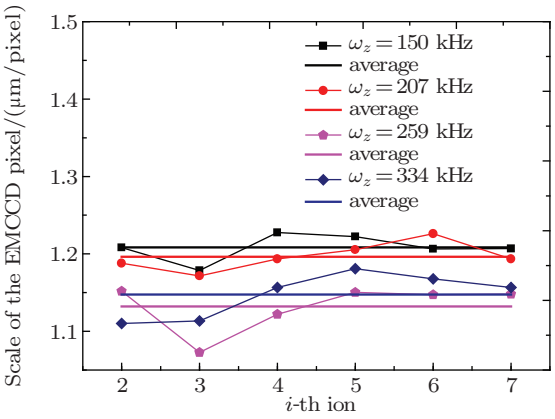


Fig. 5. (colour online) Calibration of the scale of a pixel in EMCCD. The distances between the first ion and the other ions (from the second to the seventh are labeled as 2, 3, . . ., 7 in the horizontal axis) were both theoretically solved and experimentally measured from the EMCCD images. The scale is about 1.17 μm per pixel.

We exemplify seven ions trapped stably as a linear chain in Fig. 4, where the images are taken under different axial secular frequencies. The separation of the ions could be measured by pixels in the EMCCD and the axial secular motion frequency is measured by adding a tickle signal on the endcap.[11] The real separation can be obtained by solving Eq. (7) using the optimization method. We have compared the calculated results with the measured data in Fig. 5 with the scale 1.17 μm/pixel. Because the size of one pixel on the EMCCD is 16 μm, and the image of the ions is magnified by 15 times, we know that a single pixel corresponds to the real size 1.07 μm. As a result, we obtain the angle between the trap axis and the imaging system to be

$$\theta_v = \arcsin\left(\frac{1.07}{1.17}\right) = 66.1^\circ.$$

These data are used to calculate the geometrical factors of the DC electrodes.

3.2. Measurement of the geometrical factors

The axial geometrical factor κ can be obtained by fitting the relationship between the axial secular motion frequency and the endcap voltage using Eqs. (5) and (6). The measurement in Fig. 6 gives $\kappa = 0.1143(0.0001)$.

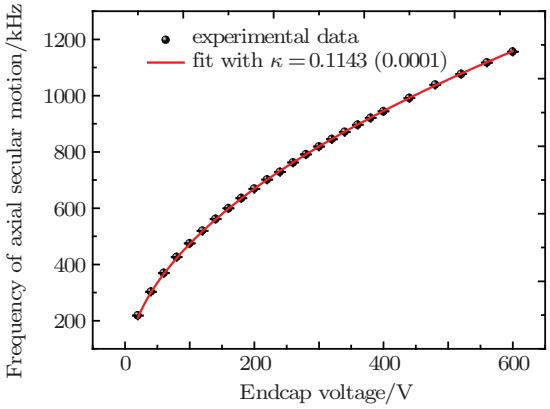


Fig. 6. (colour online) Secular motion frequency is measured under different endcap voltages by adding a tickle signal to the endcaps. Fitting to Eq. (6) gives $\kappa = 0.1143$.

In order to obtain the DC geometrical factors for the compensation electrodes, we deliberately shifted the ions by applying different voltages on the compensation electrodes. The displacements and the corresponding voltages were recorded for calculating the DC geometrical factors. The experimental data and the results shown in Figs. 7(a) and 7(b) present us with $\alpha_{c1} = 0.0080$ and $\alpha_{c2} = 0.0064$.

In order to gain more information about the axial stray static field, we have also measured $\alpha_{\rm ec}$. When endcap electrode 1 was held at 20 V and the endcap electrode 2 varied around 20 V, the displacement was recorded in Fig. 7(d), which means $\alpha_{\rm ec}$=0.0273.

Since these geometrical factors are deduced from the displacements of the ions, the precision of the results is limited by the resolution of our imaging system (about 1 μm). We have tried to reduce the limitation by carefully adjusting the voltage to locate each ion at the exact position on the EMCCD, which leads to a fitting error of less than 0.001.

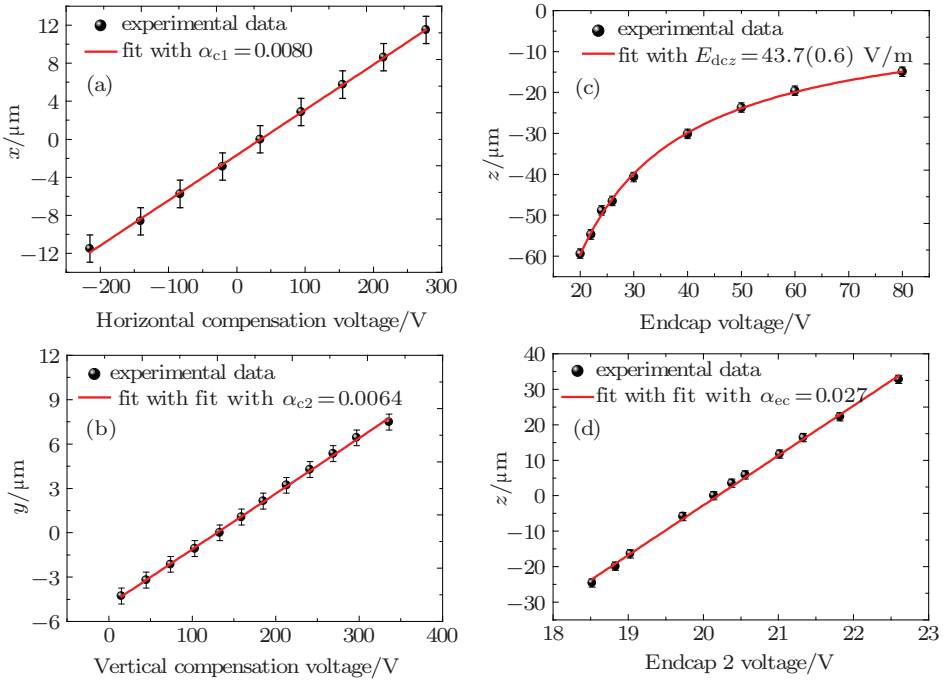


Fig. 7. (colour online) Displacements of the ion in different cases, where the error bar is due to the resolution of the imaging system. (a) Displacements in $\hat{x}'$ direction caused by the compensation electrode 5, (b) displacements in $\hat{y}'$ direction caused by the compensation electrode 6, (c) displacements in $\hat{z}$ direction caused by the stray field under different endcap voltages, and (d) displacements in the $\hat{z}$ direction caused by the endcap electrode 2 with electrode 1 at 20 V.

3.3. Measurement of the stray static fields and the endcap misalignment

We have also varied the voltages on the two endcap electrodes simultaneously and compensated the micromotion in the $\hat{x}'$ and $\hat{y}'$ directions. As shown in Fig. 8, the compensation voltages are varied with the changes of the endcap voltages, indicating misalignment of the endcaps. The stray static electric field and the size of misalignment of the endcap in $\hat{x}'$ and $\hat{y}'$ directions can be deduced by fitting the obtained data using the definitions of $E_{dc2x'}$ and $E_{dc2y'}$. From Fig. 8, we can know the pure effect of the stray field by considering a zero endcap electrode voltage and also know the misalignment of the endcaps by the slope of the line.

Figure 8 also indicates that our employed photoionization has largely suppressed the patch effect and the deposit of the electrons on the electrodes since our observation of the stray field varied only for a few volts per meter during the period of two hours, where the stray field in $\hat{x}'$ direction is varied from 195.4 V/m to 192.0 V/m and in $\hat{y}'$ direction varied from 53.0 V/m to 46.6 V/m. Moreover, the endcap electrode 2 deviated from the trap axis due to misalignment was estimated to be $\Delta x'_{ec2} = -47$ μm and $\Delta y'_{ec2} = 105$ μm. Although this deviation in $\hat{y}'$ direction could be verified by the image of the endcaps on the EMCCD, it is impossible to observe the deviation in the $\hat{x}'$ direction directly. The misalignment could be hopefully reduced by more careful work in the manual assembly.

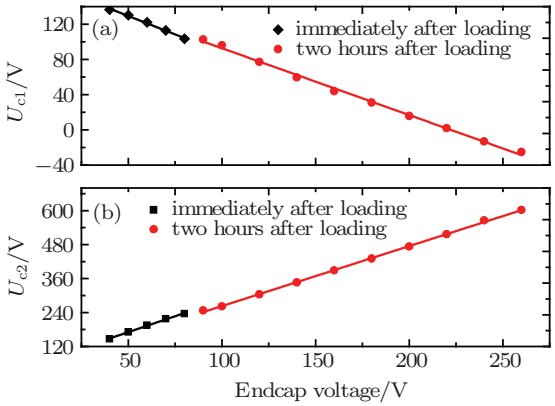


Fig. 8. (colour online) The compensation voltages with respect to the endcap voltages, where each data point is obtained using the cross-correlation method and after compensation to $\beta < 0.005$. The black points are obtained immediately after loading, and the red ones are obtained two hours later. Panels (a) and (b) are for the compensation voltages in the $\hat{x}'$ and $\hat{y}'$ directions, respectively.

The stray field in the $\hat{z}$ direction is derived by the measured displacements under different axial secular frequencies ω_z. Figure 7(c) shows a stray field of −43.7 V/m in $\hat{z}$ direction, which is large enough

to push the ions away from the trap center by several tens of μm. This field can be compensated by applying a voltage on endcap 1 higher than on endcap 2 by 4.00 V.

3.4. Detection of the effect due to the RF inductive voltage

In order to detect the excess micromotion caused by the RF inductive voltage, we have changed the filter network of the compensation electrodes to form different RF inductive voltages. Then the excess micromotion was minimized by cross-correlation method. Under this condition the suppressed β is attributed to the RF inductive voltage. The results given in Fig. 9 demonstrate that, when the inductive voltage is suppressed to be less than 1 V, the modulation of the fluorescence signal by RF is negligible to the accuracy of $\beta < 0.01$. When the inductive voltage is adjusted to 8 V, the value of β is measured to be 0.07, which is 6.5 times larger than that expected from Eq. (20). This mismatch indicates that the geometrical factor for the compensation electrodes in the RF situation is larger than what we have measured in the DC situation by 6.5 times.

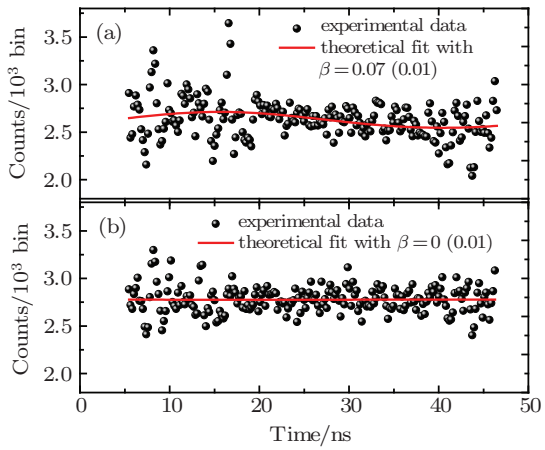


Fig. 9. (colour online) Typical cross-correlation signal obtained by laser beam 1 or beam 2, where panel (a) is obtained by compensating the static stray field to the best under the 8-V RF inductive voltage in both compensation electrodes; panel (b) is obtained by compensating the static stray field to the best under the RF inductive voltage less than 0.8 V.

3.5. Estimate of the temperature of the cooled ions

The trapped ion temperature is usually measured by the relative sideband intensity of the quadrupole transition. In our case, this could be done by using a narrow band 729-nm laser based on the resolved sideband transition.[17] However, since the linewidth of our 729-nm laser is still not satisfied for the resolved sideband transition, we have made a coarse estimate of the ion temperature following the method in Refs. [17] and [18]. After compensating all these negative effects, we measured the linewidth with different 397-nm radiations between 4 μW and 45 μW. We fit the experimental data by Lorentz fitting. This is because the Gaussian component due to Doppler broadening made negligible contribution in our spectra, which results in a the Lorentz-shape profile. A typical excitation spectrum given in Fig. 10 corresponds to the cross-correlation signal with $\beta = 0$ (0.01) in Fig. 9(b), where the intensity of 397-nm laser is 4 μW.

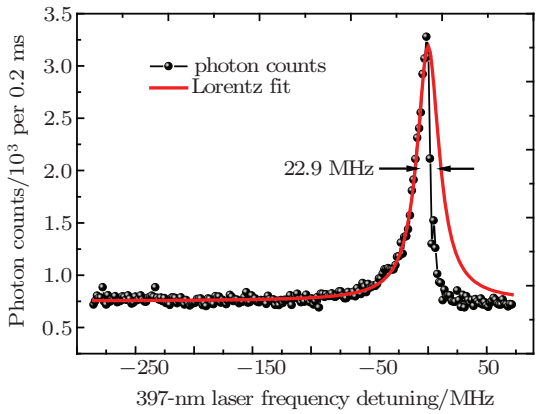


Fig. 10. (colour online) Typical excitation spectrum with a 4-μW 397-nm laser for a single ion when the stray field has been compensated in three dimensions and the inductive voltage has been suppressed to be less than 0.8 V. Since the residual Doppler broadening is very small, Lorentz fitting is used to estimate the linewidth. The drop-off of the fluorescence after the peak is due to the heating of the ion by the laser if the laser frequency is larger than the ion rest-frame resonance frequency.

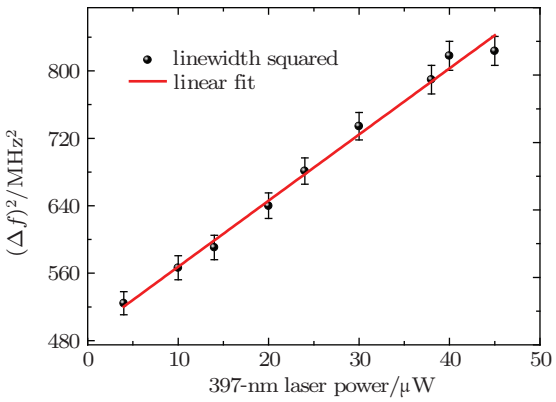


Fig. 11. (colour online) The linewidth squared versus 397-nm laser power due to power broadening of the excitation spectrum, where each point is taken from the Lorentz fitted results of different laser scans. From the fitting, the zero power broadening linewidth can be determined.

The linewidth square $(\Delta f)^2$ is fitted linearly with respect to the 397-nm laser power in Fig. 11, and a linewidth without the power broadening was obtained, by extrapolating to zero intensity, to be 22.1 (+0.6) MHz. The natural linewidth of the $^{40}Ca^+$ ion is about 20.7 MHz (22.3 MHz used in Ref. [17], but not suitable for our setup because it is even larger than the measured data). If we attribute the difference between the measured data and the natural linewidth to the residual Doppler broadening, the effective temperature of a single ion is estimated to be 0.6 mK, which is close to the Doppler cooling limit ($\sim$ 0.5 mK).

4. Discussion and conclusion

The sideband cooling works only after the trapped ion has been confined in the Lamb–Dicke regime, corresponding to $\eta\langle 2n_i+1\rangle^{1/2} \ll 1$ (Ref. [19]) with the Lamb–Dicke parameters $\eta = k\sqrt{\hbar/2m\omega_i}$ and the wave vector k. In what follows, we assess the effective temperature caused by the residual negative effects, specifically the excess micromotion using typical trap parameters $\omega_x = \omega_y = 1.2$ MHz, $\omega_z = 0.5$ MHz, and $q_x = -q_y = 0.17$.

The Doppler-cooling limit is 0.5 mK for $^{40}Ca^+$ in our experiments.[19] This implies that the minimum average quantum numbers of Doppler-cooling $\langle n_i\rangle$ are about 3.8 and 10.0 for the radial and axial directions, respectively. For the 729-nm quadrupole transition, η is about 0.14 in the axial direction and 0.088 in the radial direction, and thereby the Lamb–Dicke regime for the quadrupole transition requires $\langle n_r\rangle \ll 64$ and $\langle n_z\rangle \ll 25$. As a result, the measured residual 0.6 mK can be expressed as $\langle n_z\rangle \sim 13 < 25$, and $\langle n_r\rangle \sim 6 \ll 64$, which means that the trapped ions are fully within the Lamb–Dicke regime after the compensation is accomplished. A more precise estimate will be carried out by resolved sideband transition after our 729-nm laser is qualified for the narrow band linewidth.

We assess below the limitation of the method we have taken for detecting and compensating for the imperfections of the linear trap. Considering the micromotion caused by the stray field in the radial direction, we find that, the residual field of 0.011 V/m in $\hat{x}'$ or $\hat{y}'$ direction due to 10-mV noise of the voltage source leads to an extra temperature less than 0.1 μK. However, the cross-correlation method can only detect β (Eq. (20)) with the error on the order of 0.01, which means the residual extra temperature is less than 78 μK.

A phase shift of 0.05° causes an extra temperature 0.5 mK. After using cross-correlation method, no phase shift was found in our experiment, which means the corresponding extra temperature is less than 1 μK.

Our experimental results also indicate that the inductive voltage should be suppressed to be less than 1.7 V for ensuring that the temperature isless than the Doppler-cooling limit. In fact, by carefully choosing the optimal capacity set between the DC electrodes and the RF ground, we may suppress the inductive voltage to be less than 0.8 V, corresponding to an extra temperature 74 μK.

Adding all these effects and including 0.5 mK due to recoil energy, we obtain the temperature of our trapped ions to be 0.65 mK, which matches our measured data quite well.

In conclusion, the origin and the suppression of the excess micromotion in the linear ion trap have been studied both theoretically and experimentally, where the static stray field and the geometric factors of the DC electrodes were measured and the misalignment of the endcaps was estimated. Since the excess micromotion in three dimensions are almost suppressed, the ions are fully within the Lamb–Dicke regime.

References

[1] Blatt R and Wineland D J 2008 *Nature* **453** 1008
[2] Monz T, Schindler P, Barreiro J T, Chwalla M, Nigg D, Coish W A, Harlander M, Haensel W, Hennrich M and Blatt R 2011 *Phys. Rev. Lett.* **106** 130506
[3] Zheng X J, Cao S, Fang M F and Liao X P 2008 *Chin. Phys.* B **17** 431
[4] Zheng S B 2005 *Chin. Phys.* **11** 2222
[5] Xu Y Y, Zhou F, Zhang X L and Feng M 2010 *Chin. Phys.* B **19** 090317
[6] Cirac J I and Zoller P 1995 *Phys. Rev. Lett.* **74** 4091
[7] Stenholm S 1986 *Rev. Mod. Phys.* **58** 69
[8] Wineland D J and Itano W M 1979 *Phys. Rev.* D **20** 1952
[9] Monroe C, Meekhof D M, King B E, Jefferts S R, Itano W M, Wineland D J and Gould P 1995 *Phys. Rev. Lett.* **75** 4011
[10] Xie Y, Zhou F, Chen L, Wan W and Feng M 2011 *Chin. Phys. Lett.* **28** 093201
[11] Zhou F, Xie Y, Xu Y Y, Huang X R and Feng M 2010 *Chin. Phys.* B **19** 113206
[12] Zhou F, Xie Y, Xu Y Y, Huang X R and Feng M 2010 *Chin. Phys. Lett.* **27** 123203
[13] Berkeland D J, Miller J D, Bergquist J C, Itano W M and Wineland D J 1998 *J. Appl. Phys.* **83** 5025
[14] Steane A 1997 *Appl. Phys.* B **64** 623
[15] James D F V 1998 *Appl. Phys.* B **66** 181
[16] Donald C 2000 *Development of an Ion Trap Quantum Information Processor* Ph. D. Thesis (Oxford: University of Oxford)
[17] Urabe S, Watanabe M, Imajo H, Hayasaka K, Tanaka U and Ohmukai R 1998 *Appl. Phys.* B **67** 223
[18] Nagourney W, Janik G and Dehmelt H 1983 *Proc. Natl. Acad. Sci. USA* **88** 643
[19] Wineland D J 1987 *Phys. Rev.* A **36** 2220